FIRST ASSESSMENTS OF THE SEISMIC RESPONSE OF THE CRUAS BASE ISOLATED NPP (SMATCH Benchmark)

Christian F. Engelke[1], Ludwig Bahr[2], Mohamed Zouatine[3], Hamid Sadegh-Azar[4]

[1] Research Assistant, University of Kaiserslautern-Landau (RPTU), Germany
  (christian.engelke@bauing.rptu.de)
[2] Expert Reactor Safety Research, GRS, Köln, Germany (ludwig.bahr@grs.de)
[3] Research Assistant, University of Kaiserslautern-Landau (RPTU), Germany
[4] Head of Department, University of Kaiserslautern-Landau (RPTU), Germany

ABSTRACT

The paper aims to simulate the response of the Cruas-Meysse Nuclear Power Plant (NPP) under seismic loading. The work is part of the 3rd phase of the SMATCH benchmark (2023), which is organized by EDF (Électricité de France) and IRSN (Institut de Radioprotection et de Sûreté Nucléaire) now ASNR (L'Autorité de Sûreté Nucléaire et de Radioprotection), under the umbrella of OECD NEA (Nuclear Energy Agency). Modal analyses and linear transient time-history simulations are performed. The latter is compared to measured accelerograms recorded during the Le Teil earthquake 2019. The simulation results show good overall agreement with the measurement data. While some discrepancies are observed in the vertical direction and in the high-frequency range of the horizontal direction, the linear transient time-history analysis yields very good results in the low-frequency domain of the horizontal direction.

INTRODUCTION

The structure under investigation is Cruas-Meysse NPP, situated in the south-east of France on the banks of the river Rhône. It is operated by EDF. Among all the NPPs in France, only the Cruas-Meysse NPP is built on seismic base isolation. On November 11, 2019, a 4.9 magnitude (Mw) earthquake occurred at a distance of 15 km from the NPP site, which was later called Le Teil earthquake based on the geographical location of the epicenter. The ground and in-structure response were recorded during the event at the NPP site as well as at several locations nearby; the seismic simulation results were henceforth compared against measurement data. More details about the event and the Cruas-Meysse NPP can be found in Viallet et al. (2022).

SIMULATION MODEL

The seismic response of the building structure is simulated with the finite element program Code_Aster version 15.6.0 developed by EDF (2022). The finite element mesh provided by the benchmark organizers is utilized in the simulations. It contains soil springs, lower raft, the base isolators, the upper raft and on top of those two reactor buildings connected by auxiliary buildings. The base isolators are modelled by beam elements with a homogenized stiffness and connect the lower with the upper raft, which are modelled with shell elements. One reactor building and the auxiliary buildings are modelled with shell elements. The second reactor building, and several auxiliary buildings are represented by simplified mass-stick-models. The mesh has a total of 115 000 nodes and about 658 000 active degrees of freedom.

Because most of the auxiliary buildings are not in the focus of the investigations, the mesh of those buildings was further simplified. All nodes and beam elements representing the respective mass-stick-models of the auxiliary buildings BD1, BD2, BD5, BD6 and BD7 were each replaced by a 0D element at the center of gravity. The finite element model of Cruas-Meysse NPP is shown in Figure 1. The modelling

of the base isolators plays a critical role in determining the structural response of the simulation model, and the soil can also have a noticeable influence on the structural response. The modelling approaches for both the base isolators and the soil are therefore described in detail in the following sections.
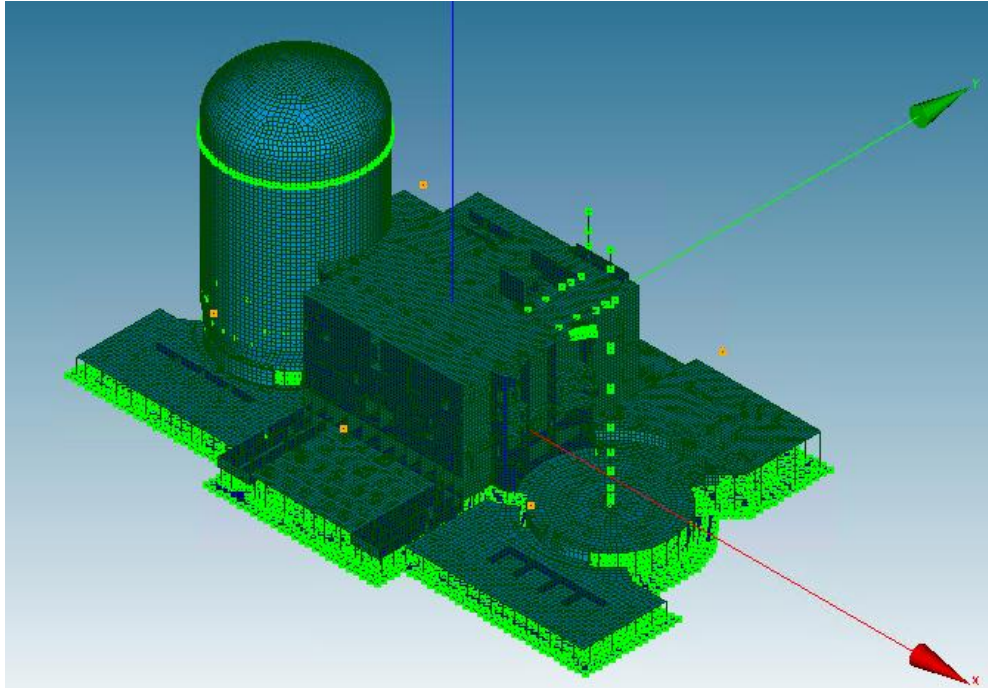

Figure 1. Finite element model of Cruas-Meysse NPP. 0D-Elements that substitute parts of the auxiliary buildings are shown as orange dots.

Base isolation

There are 1812 seismic isolators installed between the upper and lower raft. The isolators are installed on 401 different support devices, which consist of a different number of pads. There are supports with two pads, four pads and eight pads. In the simulation model, the isolators were modeled as spring-damper elements. The stiffness and damping values were derived from measurements of the shear modulus as a function of progressive distortion and aging. The table provided by the benchmark organizers contained the shear modulus for progressive distortions over various years but contained no value for the year 2019 and the distortion experienced during the Le Teil earthquake. The latter is approximated by the ratio of the maximum recorded displacement and the total height of the elastomeric part of the isolators of 40.5 mm.

Due to the absence of a shear modulus value at this level of distortion, the shear modulus G was interpolated for the required range. For this purpose, the available shear moduli from various distortions and years were first converted to shear moduli for the year 2019 using an aging curve. An approximation proposed by Simo and Taylor (1983), which describes the reduction in stiffness of viscoelastic materials, such as elastomers, under progressive distortion, was then selected. The shear modulus G is defined as the product of the initial shear modulus G_0 at zero distortion ($\gamma = 0$) and a damage function describing the decay as a function of distortion.

$$G = G_0 \left[\beta + (1 - \beta) \frac{1 - e^{-\varphi_D/\alpha}}{\varphi_D/\alpha} \right] \tag{1}$$

2

Here, the parameter β ranges between zero and one and the parameter α is a positive real number. The factor φ_D derives from the deformation behavior of the elastomer and is approximated by the distortion value according to Simo and Taylor (1983) and Ogden (2003) through

$$\varphi_D = \sqrt{2}\,\gamma\,\sqrt{1 + \frac{1}{3}\gamma^2} \tag{2}$$

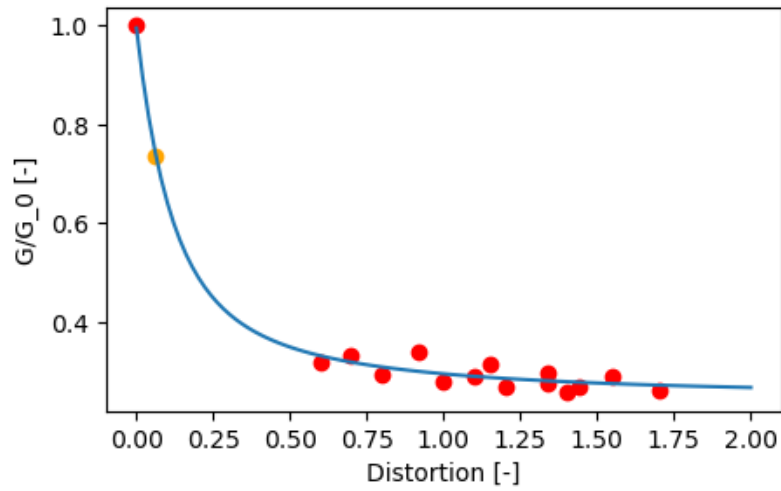A curve fitting of equation (1) gives parameter values of α and β. The resulting fit is displayed together with the measurement data in Figure 2.

Figure 2. Shear modulus G/G_0 as a function of distortion. The red dots represent the experimental data of the shear modulus transferred to the year 2019 with the help of the aging curve. The shear modulus value employed in the simulations is marked in orange.

For the calculated distortion value achieved in the Le Teil earthquake, we arrive at a shear modulus of $G/G_0 = 0.74$. The horizontal stiffness K_h and vertical stiffness K_v of the base isolators can be calculated by

$$K_h = \frac{A\,G}{T} \tag{3}$$

$$K_v = \frac{A\,E_c}{T} \tag{4}$$

Where T is the total thickness of the elastomeric layers of the bearings, and $A = a \cdot b$ the cross-sectional area of the rectangular isolators with width a and length b. The effective compression modulus E_c, which is calculated from a single elastomeric layer of width a and thickness t according to Eggert and Kauschke (2003) by

$$E_c = 3\,G\left(\frac{a}{t}\right)^2 v_3 \tag{5}$$

For a bearing with quadratic cross-section, i.e. a/b = 1, the parameter v_3 is equal to 1.4. For the given dimensions the vertical stiffness is around 500 times the size of the horizontal stiffness. A value of 7% of critical damping is applied to both horizontal directions, whereas a value of 2% of critical damping is applied in vertical direction.

Soil modeling

The benchmark organizers provided a soil stratigraphy at the Cruas-Meysse NPP site with values of density, wave propagation velocity and Poisson's ratio as a function of depth. The soil is represented in the finite element model through linear springs and dampers in x-, y- and z-direction.

To calculate the stiffness of the springs, at first, the maximum shear modulus $G_{i,max}$ of each individual layer i is evaluated from the density and the shear velocity of each layer. Based on the maximum displacement of the structure and the stiffness of the isolators, the maximum shear force was calculated. Using this shear force and an estimated rectangular raft base area, the shear stress τ exerted on the ground was subsequently determined. The distortion γ can be calculated as the ratio of shear stress τ and maximum shear modulus G_{max}. With these distortions, we calculated the ratio $G_i/G_{i,max}$ to determine the adjusted G_i values for each layer i. An iteration of this inherently iterative process was omitted, as it would have had only a minor impact on the results. The calculated shear moduli G_i increases with depth. Since the distortion is very low in the stiffer lower soil layers, $G_i/G_{i,max}$ equals 1.0 for these layers.

The stiffness of the upper layers was calculated similar to the stiffness of the Isolators, while the stiffness of the inhomogeneous lower soil layers was calculated according to FEMA P-2091 (2020). According to Waas et al. (1988) the stiffness of inhomogeneous soil profiles can be estimated using the shear modulus at a specific depth. This depth is frequency dependent. It was chosen to use the shear modulus at a depth of 70 m. The stiffnesses of the different soil layers were afterwards combined.

The damping was calculated similarly to the stiffnesses of the upper layers, using the distortion of each layer and the provided data. To combine these values into a total damping value ξ, the damping coefficients ξ_i were weighted by height h_i and distortion γ_i of each layer i

$$\xi = \frac{\sum_i \gamma_i \, h_i \, \xi_i}{\sum_i \gamma_i \, h_i} \tag{6}$$

This resulted in a damping of 4% for the soil. With the stiffness and mass of the structure, the critical damping and the damping values for each coordinate direction were estimated for each coordinate direction.

RESULTS

First a modal analysis of the model was performed and compared to provided data. This is followed by a linear transient time-history analysis.

Modal analysis

Modes in a range from 0.1 to 5 Hz are calculated. The modes with the most mass participation are the second mode with a mass participation of 80% in x-direction and 3% in y-direction as well as the third mode with a mass participation of 3% in x-direction and 85% in y-direction. The mode shape of the second mode is displayed in Figure 3, the mode shape of the third mode in Figure 4.
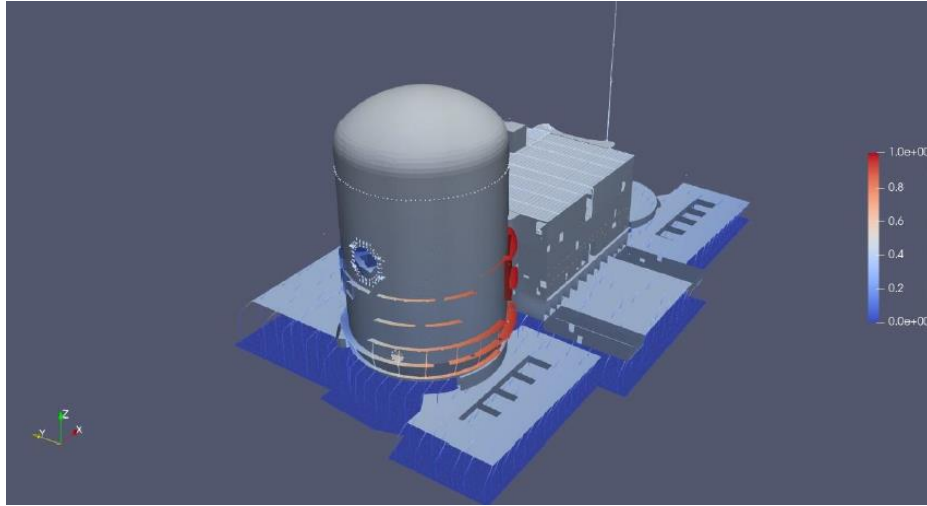
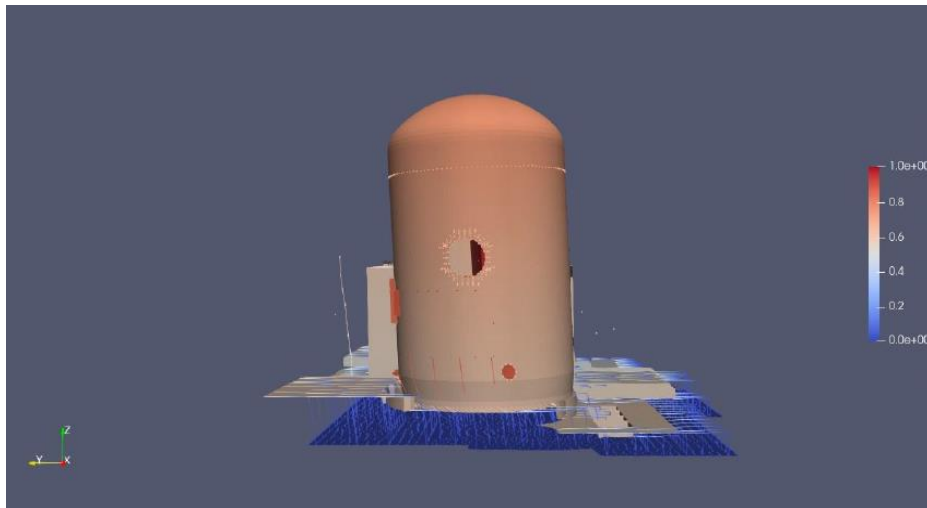Figure 3. Second mode shape at $f_2 = 1.64$ Hz.

Figure 4. Third mode shape at $f_3 = 1.64$ Hz.

Transient simulation

An implicit integration scheme with a timestep of 5 ms, which matches the timestep of the provided acceleration time signals, is used. The recorded free-field acceleration at a station nearby of the NPP is utilized to excite the model. Resulting accelerations are evaluated in a local coordinate system u,v,w with the v-direction pointing along one of the building axis, which is approximately in North North East (NNE) direction. The transient simulation is compared to synchronized system sensor recordings at three different EAU systems locations. Triaxial simulated and recorded acceleration time signals and corresponding response spectrums at sensor location EAU 001 are displayed in Figure 5 to Figure 7, those at location EAU 002 in Figure 8 to Figure 10 and those at location EAU 003 in Figure 11 to Figure 13.

The simulations at location EAU 001 show good agreement with the measured accelerations in the horizontal direction and slightly diverge in the vertical direction. This is also evident in the response spectra. In the horizontal direction, only minor deviations are observed between the simulations and the measurements. The first peak is accurately captured, especially in the direction v, where the peaks align precisely. However, a second, smaller peak observed in the measurements at approximately 9 Hz is not reproduced in the simulations.

At location EAU 002, it is evident that the higher-frequency components of the horizontal vibrations are not sufficiently represented in the simulations, whereas there is good agreement in the lower-frequency range.

Location EAU 003 shows the best overall agreement between simulation and measurement results in both horizontal and vertical directions. The response spectra of the simulated and measured accelerations exhibit only minor deviations.

Simulated horizontal accelerations

Recorded horizontal accelerations

Simulated vertical acceleration

Recorded vertical acceleration
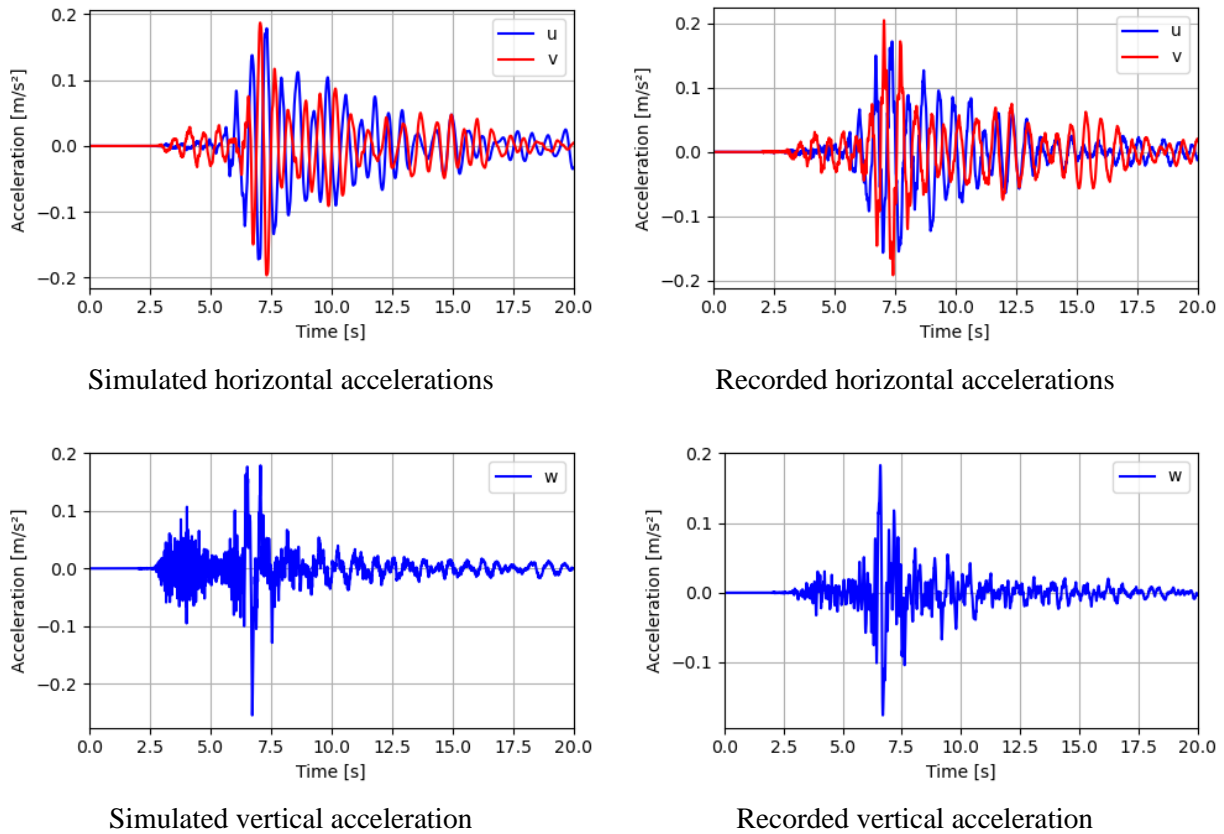
Figure 5. Recorded and simulated acceleration time signals at system sensor EAU 001.
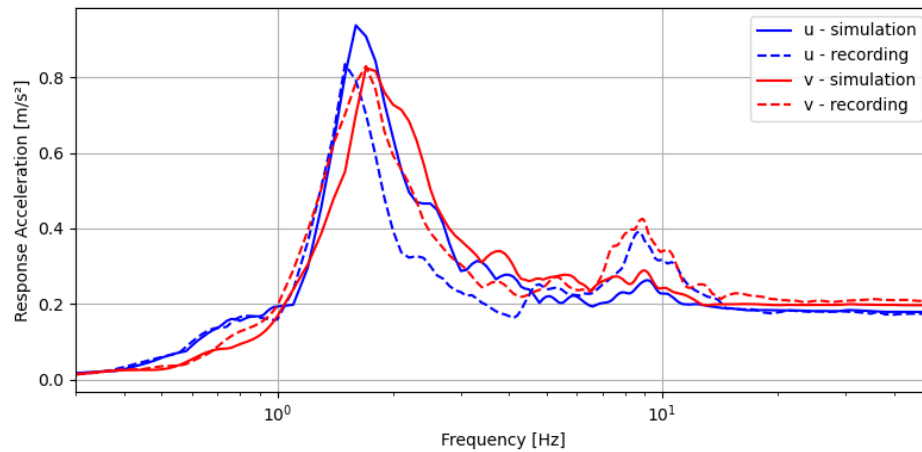
Figure 6. Response spectra for simulated and recorded horizontal time-histories at system sensor EAU 001.
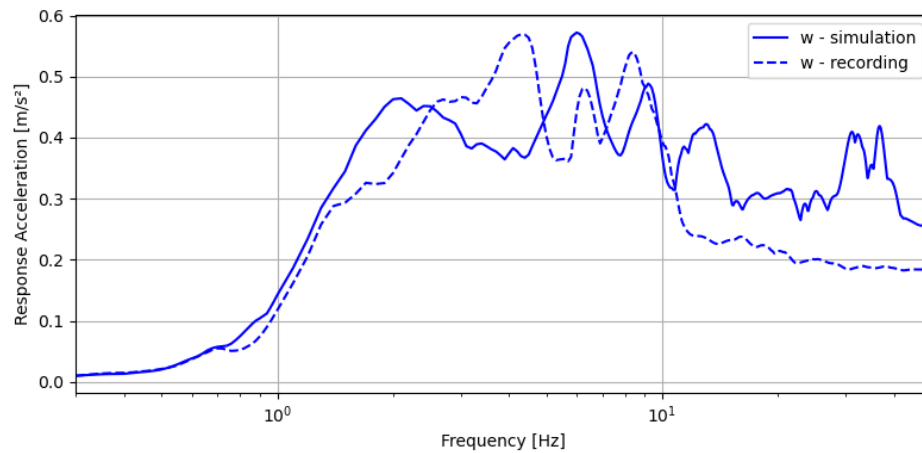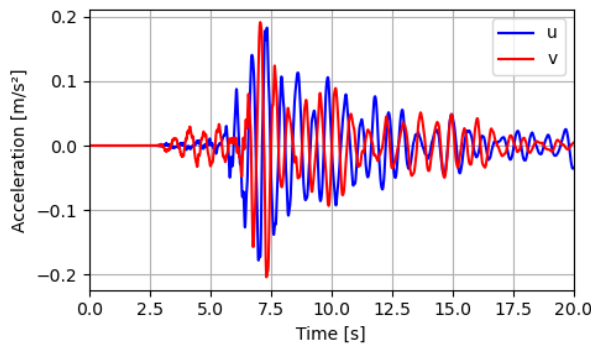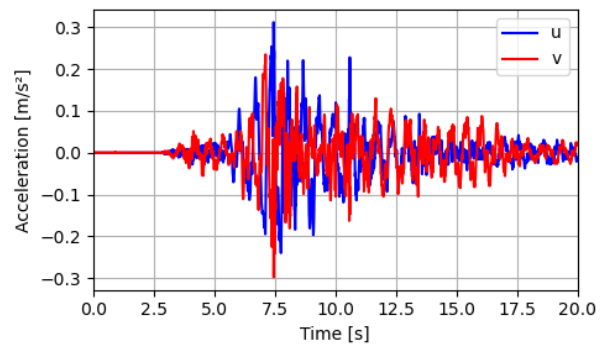

Figure 7. Response spectra for simulated and recorded vertical time-histories at system sensor EAU 001.

Simulated horizontal accelerations
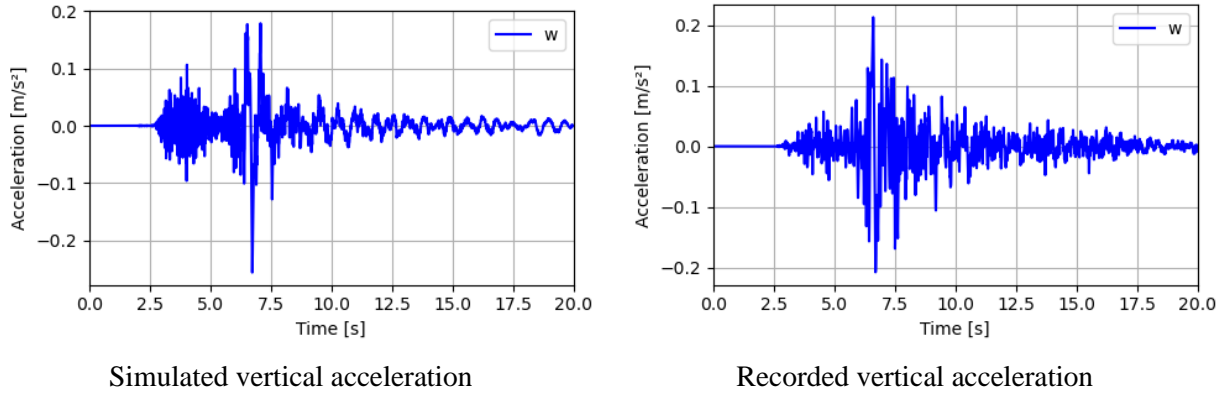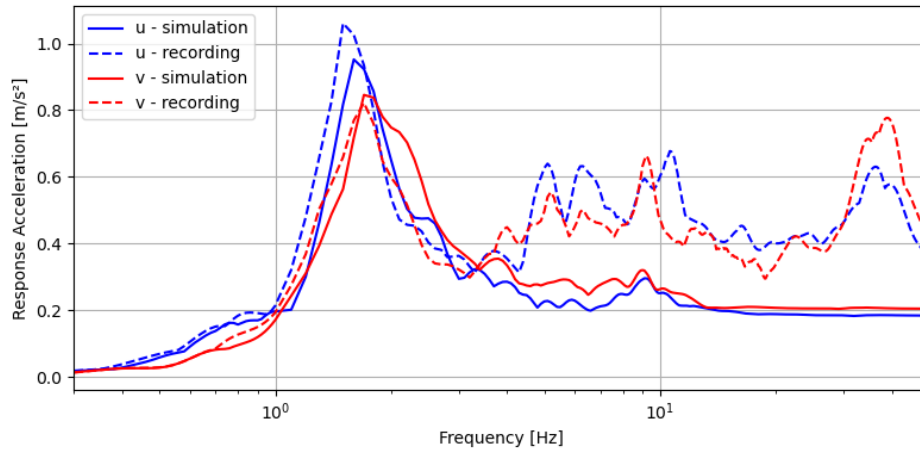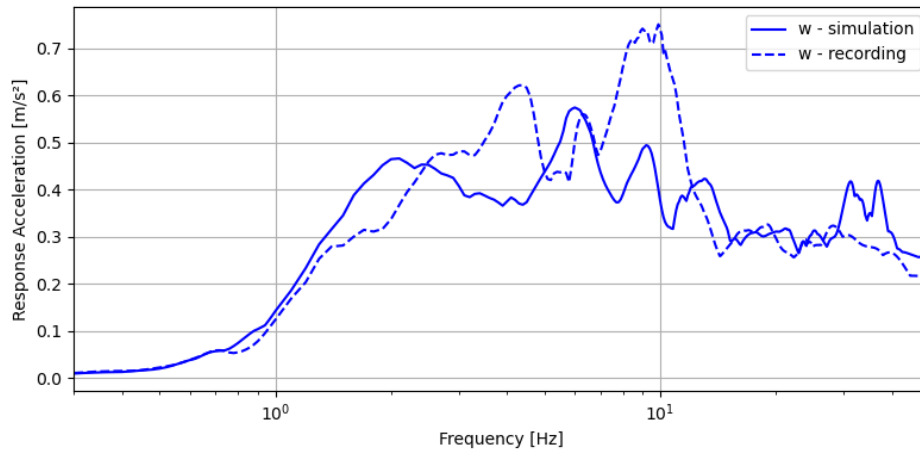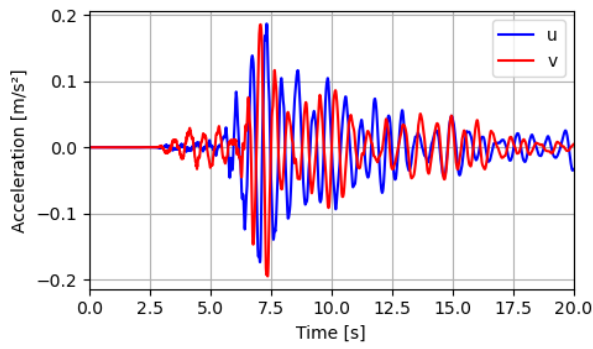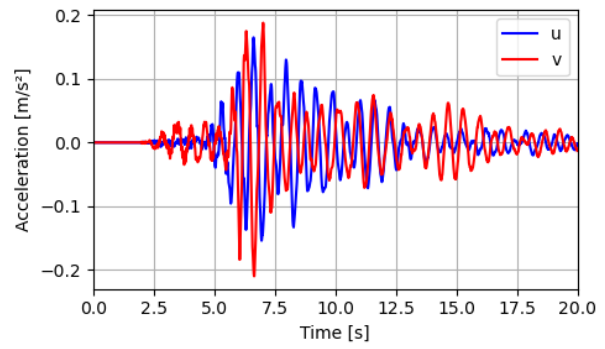

Recorded horizontal accelerations

7

Simulated vertical acceleration   Recorded vertical acceleration

Figure 8. Recorded and simulated acceleration time signals at system sensor EAU 002.

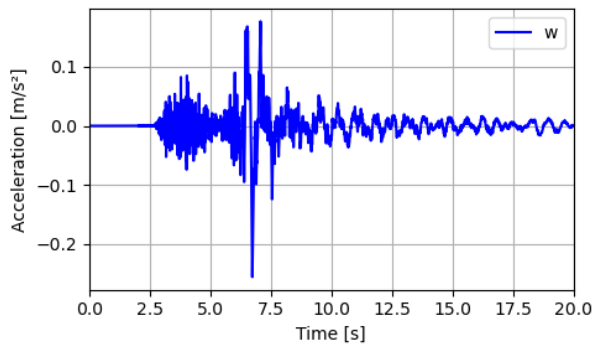Figure 9. Response spectra for simulated and recorded horizontal time-histories at system sensor EAU 002.

Figure 10. Response spectra for simulated and recorded vertical time-histories at system sensor EAU 002.
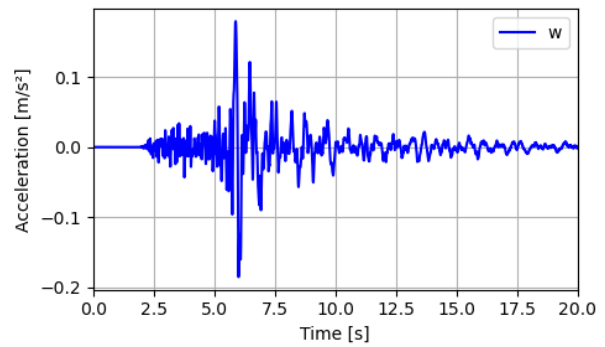
8

Simulated horizontal accelerations

Recorded horizontal accelerations

Simulated vertical acceleration

Recorded vertical acceleration

Figure 11. Recorded and simulated acceleration time signals at system sensor EAU 003.
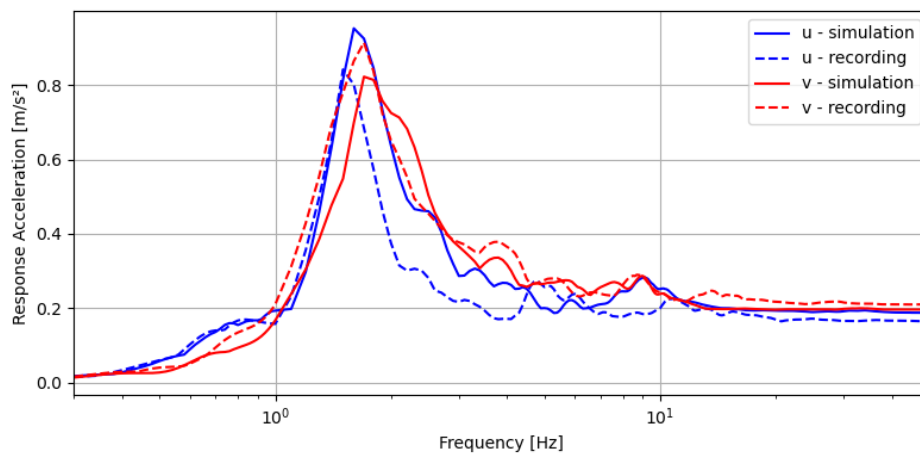

Figure 12. Response spectra for simulated and recorded horizontal time-histories at system sensor EAU 003.
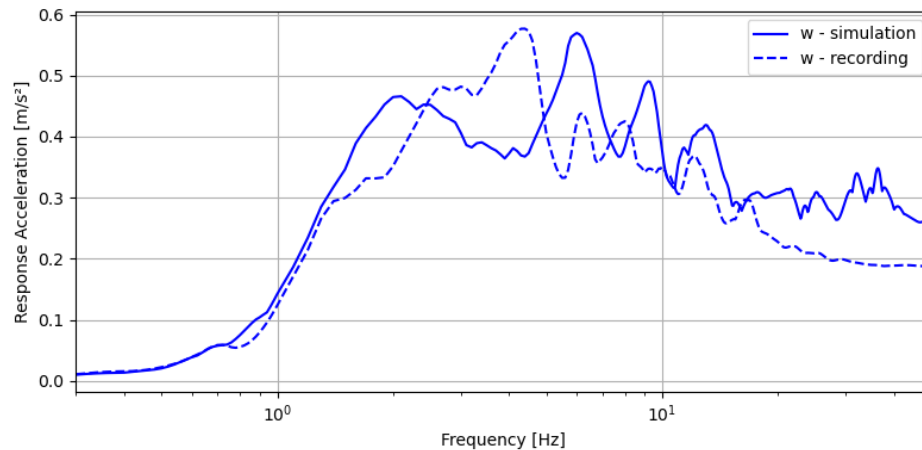
Figure 13. Response spectra for simulated and recorded vertical time-histories at system sensor EAU 003.

CONCLUSION AND OUTLOOK

A satisfying level of accuracy is achieved in both the modal analysis and the transient simulations. While certain discrepancies persist in the vertical direction and in the high-frequency range of the horizontal direction, the linear transient time-history analysis shows very good agreement with the measurements in the low-frequency range of the horizontal direction. At location EAU 002, where high-frequency components dominate, the overall deviations are more pronounced. In contrast, location EAU 003 is primarily influenced by low-frequency accelerations, resulting in the best agreement between simulation and measurement. The observed differences will be subject to further investigation. A focus of future work will be methods to include soil-structure-interaction in more detail and the nonlinearity of the base isolation.

REFERENCES

EDF, IRSN, OECD NEA (2023). *SMATCH Benchmark,* Homepage: https://www.smatch-benchmark.org.
EDF (2022). *Code_Aster*, Version 15.6, Homepage: https://code-aster.org.
Eggert, H., Kauschke, W. (2002). *Structural bearings*, ISBN 3-433-01238-5, Ernst & Sohn.
FEMA P-2091 (2020). *A Practical Guide to Soil-Structure Interaction*.
Ogden, R. W. (2003). *Nonlinear Elasticity with Application to Material Modelling*, AMAS Lecture Notes.
Simo, J. C., Taylor, R. L. (1983). *A Simple 3-Dimensional Viscoelastic Model Accounting for Damage Effects*, Report No. UCB/SESM-83/10, SEMM Reports Series, UC Berkeley.
Viallet, E., Berger, J., Traversa, P., El Haber, E., Hervé-Secourgeon, E., Hervé-Secourgeon, G., Zuchowski, L., Dupuy, G. (2022). 2019-11-11 Le Teil Earthquake – The Ultimate Missing Piece of Experience Feedback Related to a Nuclear Power Plant Built on Seismic Base Isolation: A Real Earthquake. Transactions, SMiRT-26, Berlin/Potsdam, Germany, July 10–15, 2022, IASMiRT
Waas, G., Hartmann, H.-G., Werkle, H. (1988). Damping and stiffness of foundations on inhomogenous media, Proc. 9th World Conference on Earthquake Engineering III, 343–348.